ACCEPTED MANUSCRIPT
Review of Scientific Instruments
AIP Publishing
This is the author's peer reviewed, accepted manuscript. However, the online version of record will be different from this version once it has been copyedited and typeset.
PLEASE CITE THIS ARTICLE AS DOI: 10.1063/5.0191095

Exploring Mounting Solutions for Cryogenically Cooled Thin Crystal Optics in High Power Density X-ray Free Electron Lasers

Zhengxian Qu and Yanbao Ma
Department of Mechanical Engineering, University of California, Merced, CA 95343, USA

Juhao Wu
SLAC National Accelerator Laboratory, Menlo Park, CA 94025, USA
(*yma5@ucmerced.edu)

This study investigates three mounting methods—clamping, soldering, and a hybrid clamping-soldering approach—for cryogenically cooled thin diamond crystals crucial to stable X-ray Free Electron Lasers systems. While clamping methods exhibit temperature resilience and flexibility, meticulous design is required to prevent stress-induced warping and reduce thermal contact area. Soldering methods offer reliable mechanical and thermal bonding but encounter challenges due to coefficient of thermal expansion mismatches at cryogenic temperatures. The hybrid method, integrating clamping and soldering with strain relief cuts, effectively mitigates overall distortion caused by mounting and XFEL thermal loads. These findings offer a novel mounting solution for high-performance X-ray optics in XFEL research and applications, ensuring stability and optimal functionality in cryogenic conditions.

I. INTRODUCTION

X-ray Free-Electron Lasers (XFELs) [1–4] have transformed the landscape of X-ray science, starting with the inaugural XFEL facility at the SLAC National Accelerator Laboratory in 2009 [1]. These facilities have ushered in a new era of scientific exploration by providing unprecedented capabilities for probing the structure [5, 6] and dynamics [7, 8] of matter at the atomic/molecular length scale and femto/subfemtosecond time scale. XFELs achieve this by generating exceptionally bright and coherent X-ray pulses lasting mere femtoseconds [9–11]. This remarkable attribute empowers researchers to delve into the intricacies of various materials, including biological molecules, catalysts, and emerging substances.

Nonetheless, the remarkable brightness of XFELs also brings about a formidable challenge in the form of high thermal power density. This intense heat can lead to substantial temperature increases in the samples under scrutiny, as well as the optical and experimental apparatus responsible for manipulating and measuring X-rays [12–14]. These temperature fluctuations can significantly compromise data quality and the longevity of the equipment used.

Thin crystal optics are also introduced into the applications of XFELs due to their unique optical functions. For example, thin crystal optics can be used to share a single XFEL beam among multiple experiments [15, 16], allowing researchers to maximize the use of the available X-ray beam time. Thin crystal optics can also be used to detect the spectrum of the X-rays [17, 18]. In addition, thin crystal optics are used in hard X-ray self-seeding [19–21], a technique that can significantly enhance the longitudinal coherence and spectral purity of the XFEL beam.

However, the utilization of thin crystal optics introduces its own set of challenges, especially in effectively managing the heat generated by the intense X-ray beams. To efficiently dissipate this type of heat without introducing undue strain, a dependable and thermally efficient mounting design is imperative. This need becomes particularly pronounced in the context of high reptition rate operation, such as hard X-ray self-seeding at 1 MHz, where thermal power densities far surpass those encountered in other XFEL applications by several orders of magnitudes. While multiple mounting designs have been proposed and tested previously [3, 15, 21–26], comprehensive cooling strategies that align with these mounting designs have yet to be reported.

Overcoming the challenges linked to thin crystal optics requires an exploration of innovative mounting mechanisms. The development of such mechanisms promises not only to enhance the performance of thin crystal optics but also to elevate the overall capabilities of XFELs for investigating complex materials. Advanced computational methods, including finite element analysis and computational fluid dynamics, offer invaluable tools for mounting design and optimization of thin crystal optics. Furthermore, the integration of substrate materials with high thermal conductivity, such as graphene and diamond holds the potential for effective heat dissipation and strain management within crystal optics.

Consequently, this paper is dedicated to investigating two such mounting mechanisms—soldering and clamping—in response to the thermal challenges faced by thin crystal optics in XFEL applications. We shall present our discoveries regarding the mechanical and thermal behavior of these mounting designs and deliberate on their potential to enhance performance and reliability within the realm of XFEL science.

II. MOUNTING DESIGN

The fundamental aim of the mounting design is to minimize disruptions to the Bragg condition at the XFEL footprint. This disruption results from a combination of factors, including surface slope, external mounting distortion, and XFEL-induced heating disturbances [12, 13, 27]. Consequently, the mounting design should strike a delicate balance between minimized mounting-induced deformation and min-

25 August 2025 17:57:44

ACCEPTED MANUSCRIPT
Review of Scientific Instruments
AIP Publishing
This is the author's peer reviewed, accepted manuscript. However, the online version of record will be different from this version once it has been copyedited and typeset.
PLEASE CITE THIS ARTICLE AS DOI: 10.1063/5.0191095

imized thermal interface impedance. One well-established mounting method in synchrotron and XFEL beamlines is clamping [15, 22, 24–26, 28]. However, clamping thin crystals presents distinct challenges, typically requiring either the application of minimal force (on the order of 10^{-2} to 10^{-3} N) or the creation of extensive strain relief cuts on the crystal [21], hindering efficient cooling. In contrast, soldering [29] offers excellent thermal contact and mechanical bonding but poses issues related to external strain and the irreversibility of the process. As a base for comparison, the thin crystal presented in this section is without showing strain relief cuts, while the results with strain relief cuts will be presented in later sections. To comprehensively evaluate these two methods within the context of cooling design, we present designs that facilitate a fair comparison between them.

A. Clamping Design

Clamping is a common mounting method that uses precise machining without phase change or chemical reaction. It offers good thermal contact conductance (TCC) of approximately 0.5 W/(mm^2·K) for X-ray optics when using indium foil as the interstitial material [30, 31]. Additionally, clamping allows for the reuse of the crystal if necessary. However, the application of clamping to thin crystals has been limited due to strain-induced optical distortion.

Direct clamping of the crystal, even near its edges, can introduce significant strain, even for relatively thick crystals (approximately 0.5 mm). To mitigate this issue, some designs incorporate strain relief cuts, permitting clamping near one edge, as observed in the HXRSS monochromator at EuXFEL [21]. To address the strain generated by clamping and enhance thermal contact, we introduce a design similar to existing ones (see Fig. 1). The crystal used in this work (for all designs) is 5 mm by 5 mm by 100 μm. Several design features, such as rounded edges near the clamping area to avoid sharp contact with the crystal and a rounded tip tail to balance force moments, have been incorporated into the clamp design. For both the M1 bolts and clamps, we opt for SUS304 due to its strength and hardness. Consequently, when tightened, the bolts and clamps deform relatively insignificantly to prevent detachment near the front edge, thus maintaining an effective clamping contact area and mitigating intense stress. We employ two clamps to provide additional degrees of freedom for compensating dimensional and assembly tolerances. To enhance TCC and reduce the impact of surface roughness, indium foil is applied at two interfaces. The holder, for now, is a simple OFHC copper block, simplifying the study and enabling a focused analysis of the clamping mechanism. The detailed holder design should be tailored to specific system requirements.

B. Soldering Design

Soldering offers excellent mechanical and thermal bonding capabilities, boasting TCC values that can reach $1-100$ W/(mm^2·K) [32, 33]. Vacuum soldering, in particular, minimizes voids or air pockets, approaching the theoretical TCC limit. In our study, we conservatively assign a value of 1.5 W/(mm^2·K) for all soldered contacts for the convenience of analysis and discussion. Despite its potential advantages, soldering thin crystals for XFEL applications has been relatively uncommon due to the complexities of the soldering process and the resultant external strain. Factors such as surface tension of the melted solder, volume change during solidification, and coefficient of thermal expansion (CTE) mismatch contribute to this strain. To mitigate CTE-related strain issues between OFHC copper and diamond, we introduce a diamond base (which can be of lower quality) as a buffer. The thin diamond is soldered to the 1-mm-thick diamond base (10 mm by 5 mm for transverse dimensions), which is subsequently soldered to the holder (Fig. 2). Also, indium or tin-indium is selected as the solder material due to its low melting point and softness, as well as its compatibility with UHV and cryogenic temperatures. Ga-In eutectic is not selected due to its complex interaction with oxygen and OFHC copper, and additional complexity introduced by the skin layer formed in the air.

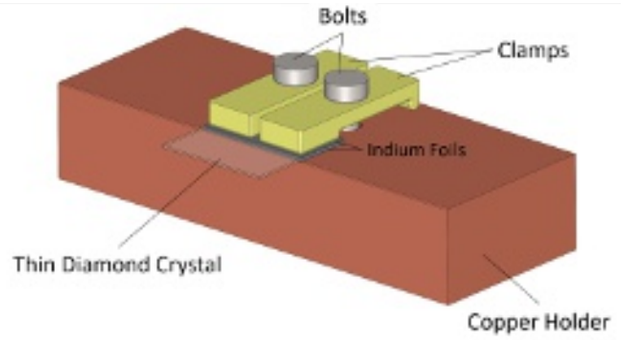

FIG. 1: The clamping design. The thin crystal optics is clamped to the dummy copper holder by two clamps and bolts, with two sheets of indium foils between the interfaces for improved contact.

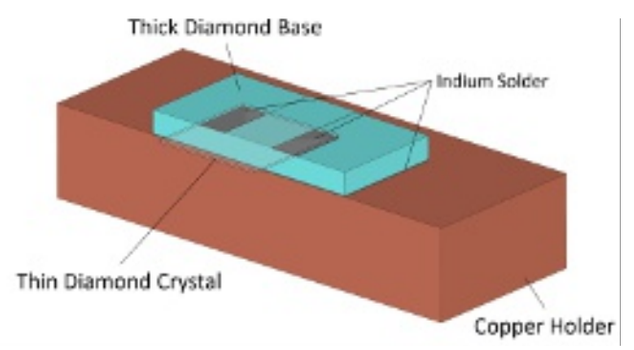

FIG. 2: The soldering design. The thin crystal is soldered to a thick diamond base (10 mm by 5 mm by 1 mm) used as a buffer, and the base is then soldered to the dummy holder.

25 August 2025 17:57:44

ACCEPTED MANUSCRIPT
Review of Scientific Instruments
AIP Publishing
This is the author's peer reviewed, accepted manuscript. However, the online version of record will be different from this version once it has been copyedited and typeset.
PLEASE CITE THIS ARTICLE AS DOI: 10.1063/5.0191095

C. Hybrid Design

This design involves both clamping and soldering approaches. Unlike the soldering design depicted in Fig. 2, here, the thin diamond device is initially soldered to a thick diamond base (same dimension as in soldering design), and the base is then clamped to a copper holder (Fig. 3). The same design features for the clamp, such as rounded contact faces and a round tip to balance out the moment, are incorporated. The clamps are oriented differently (90°rotated) to compensate the potential concave warpage of the base. This design offers increased flexibility for crystal optics reuse, as the device (comprising the crystal optics and the diamond base) can be detached from the holder.

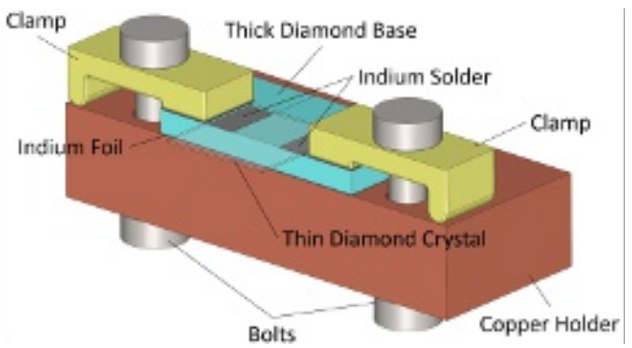

FIG. 3: The hybrid design. The thin crystal is soldered to a 1-mm-thick diamond base (10 mm by 5 mm in transverse directions) used as a buffer, and the base is clamped to the dummy copper holder.

III. NUMERICAL SETUP

In this section, we outline the numerical setup for our finite element analysis (FEA). We adopt a steady-state analysis approach for all cases, focusing on the effects of mounting while simplifying the study.

The FEA setup aligns with our previous work [34], with adjustments to bolt pretension and contact connection settings. We model clamped connections as frictional contacts with a friction coefficient of 0.2, allowing for sliding between the contact faces. To establish contact, we adjust the clamped connection pairs to touch or slightly penetrate each other, creating initial contact. We employ a symmetric behavior and augmented Lagrange formulation to balance penetration forces and resource requirements. Additionally, we utilize the default stabilization settings in the nonlinear solver control to enhance convergence. Soldered connections are represented as bonded connections.

Figure 4 illustrates the boundary conditions for our static structural analysis. A gravity force acts in the z direction, as indicated by the yellow arrow. Frictionless supports are applied to the left, back, and bottom faces of the holder, facilitating free thermal expansion. To prevent rigid body motion,

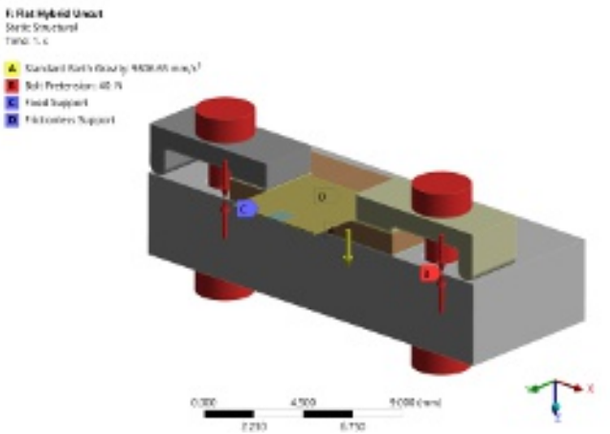

FIG. 4: Boundary conditions for finite element analysis. The gray square part marked on crystal is the optical working area (1 mm by 1 mm) where the mesh is refined to yield better results.

we fix one corner point of the holder, denoted as "D" in Fig. 4. The clamping load is simulated using bolt pretension, with each bolt carrying an individual load of 10 N for the clamped case and 40 N for the hybrid case.

In the steady-state thermal simulation, we maintain the bottom face of the holder at a constant temperature of 90 K to mimic cryogenic cooling. Heat load application follows our previous work [13] using APDL commands, with a fixed total absorbed power of 15 W. The Bragg angle is 45 degrees for 9.83 keV at the diamond (0 0 4) reflection, and the absorption length is 1.518 mm. Material properties vary with temperature, as detailed in our prior studies [12, 35]. We set the reference temperature for all components involved in soldering at 391.15 K (118°C), corresponding to the melting point of tin-indium. For other components, the reference temperature is 300 K, typical for room temperature assembly process.

For the soldered case, our simulation workflow begins with a steady-state thermal simulation to obtain the temperature field. We then import this temperature field into the static structural simulation, introducing an inhomogeneous thermal load to the model. In the case of clamped and hybrid configurations, we initially perform a static structural simulation to establish thermal contacts. We export the pressure distribution on contact faces and calculate the TCC using an in-house MATLAB code. Further details will be provided in subsequent sections. The calculated TCC, along with the deformed mesh from the static structural analysis, is incorporated into the steady-state thermal simulation to accurately model thermal contact. This process continues iteratively until converged thermal and structural fields are obtained. However, in this study, we demonstrate the process once to achieve reasonable results with affordable computational effort.

Upon completing the final simulation, we export the deformation in the z direction (u_z) and total strain (ε_{zz}) near the XFEL spot. These values are used in our in-house MATLAB code to calculate surface slope and total disturbance [27] to

25 August 2025 17:57:44

ACCEPTED MANUSCRIPT
Review of Scientific Instruments
AIP Publishing
This is the author's peer reviewed, accepted manuscript. However, the online version of record will be different from this version once it has been copyedited and typeset.
PLEASE CITE THIS ARTICLE AS DOI: 10.1063/5.0191095

the Bragg condition.

IV. MOUNTING DISTORTION

In this section, we delve into the assessment of crystal distortion following assembly at room temperature (300 K), focusing on the mounting methods without considering cooling effects. This simulation results will guide mounting design of thin-film X-ray optics.

In Fig. 5, we present the outcomes for all three designs after assembly at 300 K. For fair comparisons, we assume that the soldered case is initially soldered at 391.15 K (118°C) and then gradually cooled to room temperature (300 K). In this simulation, we operate under the assumption of ideal geometries, where the crystal surface is flawlessly flat, free of waviness, and the system is assembled with zero tolerance.

We examine a circular region with a radius five times that of the XFEL spot size ($3\sigma_x$ = 60 μm). This selection yields a circle with a 0.3 mm radius, designated as our region of interest (ROI). The center of this ROI is overlapped with the center of optical working area marked in Fig. 4, which is 0.5 mm away from the edge and on the center line.

For the flat clamped case, we observe a RMS surface slope of 1.78 μrad (varying from -3.62 to 3.58 μrad). This RMS surface slope remains within an acceptable range when compared to the Darwin width at 9.83 keV for C(0 0 4), which measures 7.56 μrad. Moreover, the total z strain (ε_{zz}) within the ROI has a RMS of 6.98×10^{-8} (varying from -1.26×10^{-7} to 1.58×10^{-8}) due to mounting, and is deemed negligible in contrast to the 7.56 μrad Darwin width.

For the flat soldered case, we observe a RMS surface slope of 9.71 μrad (varying from -19.33 μrad to 19.38 μrad. Notably, the considerable distortion here stems from the CTE mismatch between the diamond and solder. In the ROI, the mounting strain exhibits a RMS of 9.76×10^{-7} (varying from -7.19×10^{-7} to 2.24×10^{-6}), which is of the same magnitude as the Darwin width and reflects the pronounced influence of CTE mismatch on the strain field.

In the case of the flat hybrid design, the RMS surface slope is 0.80 μrad (varying from -1.60 μrad to 1.60 μrad). This result notably surpasses the soldered case due to the incorporation of clamping, which permits sliding and compensates for warpage. Mounting strain within the ROI is minimal, exhibiting a RMS of 1.93×10^{-7} (varying from 4.90×10^{-8} to 3.23×10^{-7}).

In practical applications, system geometry seldom aligns perfectly. Factors such as surface waviness, assembly errors, and component variations introduce imperfections that affect results. To account for these real-world nuances, we introduce sinusoidal profiles on the crystal's top and bottom faces in the lateral direction, with a 5 mm wavelength and a phase difference of π. This mirrors a worst-case scenario (as depicted in Fig. 5). These simulations illustrate that imperfections have a pronounced impact on the clamped case, leading to heightened surface slope and strain. It's important to note that in reality, predicting the precise surface profile can be challenging, if not impossible; thus, the sinusoidal profile serves solely to showcase the ramifications of surface waviness and tilted (WT) installation.

For the clamped case, the average surface slope increases nearly a hundredfold (RMS slope of 135.98 μrad), which could lead to significant photon energy fluctuation when the XFEL beam center jitters. This effect arises from symmetry breaking and the introduction of shear forces by the clamps, inducing bending and warpage. Conversely, the soldered and hybrid cases display greater resilience to imperfections, underscoring the advantages of soldering in this context. In the soldered case, the outcome even slightly outperforms the flat scenario, exhibiting a RMS slope of 1.39 μrad (varying from -2.34 μrad to 4.29 μrad). Meanwhile, the hybrid case yields a RMS slope of 5.78 μrad (varying from -11.46 μrad to 11.74 μrad), demonstrating its robustness in handling imperfections. All the disturbance results (surface slope and strain) are summarized in Table III.

V. THERMAL CONTACT

In this section, we evaluate thermal contact within our system for different mounting methods. It should be noted that the contact status undergoes significant changes as the system is cooled down to its operational temperature of approximately 90 K. Therefore, in our static structural simulation, we consider thermal contact at room temperature (300K) in the initial step and 90 K in the subsequent step.

The pressure distribution between the crystal/indium (C/In) interface and between the indium/copper (In/Cu) interface is displayed in Fig. 6, specifically with the flat clamped case on the left side. For soldered interface, the TCC is assumed constant and is not shown here. Notably, we observe a maximum pressure of approximately 2.43 MPa, indicative of concentrated local stress. Intriguingly, around one third of the contact surface exhibits zero pressure, suggesting that these regions do not contribute to heat transfer since they are not in actual contact. In essence, this implies that in the clamped case, the effective heat transfer area amounts to only about 67.60% of the apparent contact area in the flat clamped case. In comparison, the contact pressure distribution for the WT cases, depicted on the right side of Fig. 6, indicates an even greater loss of effective heat transfer area. Here, only approximately 4.08% of the contact area can contribute to heat transfer.

To determine the TCC, we export the pressure distribution data for the C/In and In/Cu interfaces to our in-house MATLAB code. We employ an extended Cooper-Mikic-Yovanovic model [36] for this purpose. The microhardness (H_c) of the indium foil, measured by Cai [37], is established at 19.4 MPa. TCC (h) is calculated using the following equation:

$$h = 1.25\frac{m_s}{\sigma_s}k_s\left(\frac{P}{H_c}\right)^{0.95}. \quad (1)$$

Here, $\sigma_s = \sqrt{\sigma_1^2+\sigma_2^2}$ denotes the root mean square of the surface roughness of the two contact faces, and $m_s =$

25 August 2025 17:57:44

ACCEPTED MANUSCRIPT
Review of Scientific Instruments
AIP Publishing
This is the author's peer reviewed, accepted manuscript. However, the online version of record will be different from this version once it has been copyedited and typeset.
PLEASE CITE THIS ARTICLE AS DOI: 10.1063/5.0191095

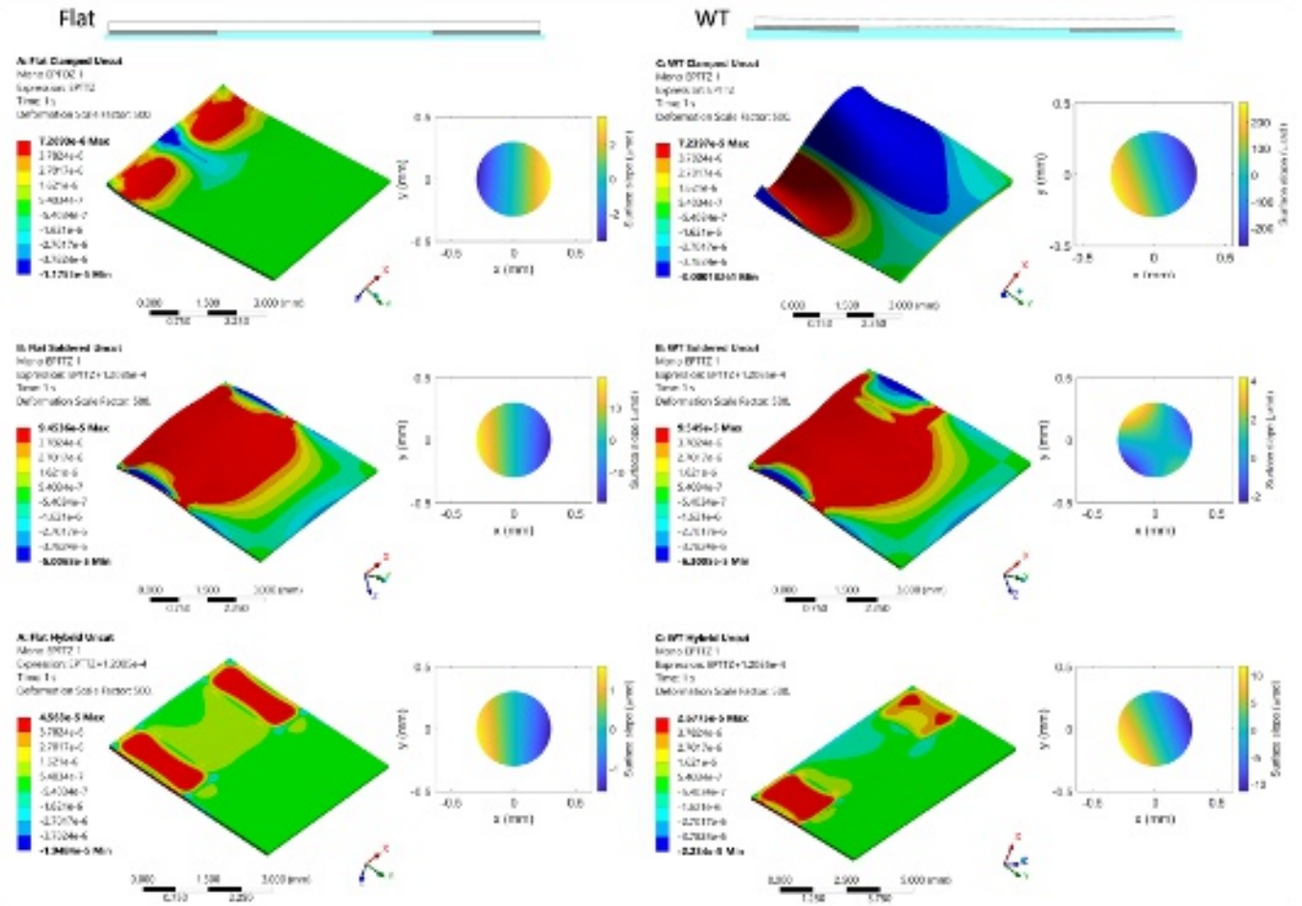

FIG. 5: Strain and surface slope for perfectly flat geometry (left column) and WT (right column) for clamped (upper row), soldered (middle row) and hybrid (lower row) cases. The colorbar for strain plot is modified to mostly show the strain within a Darwin width range of $\pm 3.78 \times 10^{-6}$. The circular region radius is 5 times of 3σ to show the surface slope near the beam center location. The strain field is offset by a reference strain (thermal strain of 1.2085×10^{-4} from 391.15 K to 300 K for soldered and hybrid cases. The crystal surface profile is also visualized in xz plane for a straightforward presentation.

$\sqrt{m_1^2+m_2^2}$ represents the root mean square of the asperity slope. The asperity slope (m) can be computed [38, 39] as $m = 0.076\left(10^6\sigma\right)^{0.52}$. Additionally, $k_s = \frac{2k_1k_2}{k_1+k_2}$ stands for the effective thermal conductivity of the contact pair. We apply Eq. (1) to the C/In, In/Cu, and clamp/indium (In/C) interfaces, respectively, as these three contact faces are highly efficient in heat transfer. All other contact faces are assigned a constant TCC value of 0.002 W/(mm^2·K) for simplicity. The resulting TCC distribution is also illustrated in Fig. 6 for clamp design as an example, since the TCC is much higher and uniform in hybrid design due to high clamping force. Once averaged over the effective area, a single TCC value is obtained and utilized in subsequent simulation steps. The average TCC for all cases are summarized in Table I.

For instance, in the flat clamped case, the effective TCC is 1.52 W/(mm^2·K) for the C/In interface between the crystal and copper holder, which is similar to TCC for soldered interface, and 13.48 W/(mm^2·K) for the WT clamped case. However, if we take average of the TCC over the apparent contact area for C/In interface, these values would reduce to 1.03 W/(mm^2·K) for the flat case and 0.55 W/(mm^2·K) for the WT case, accounting for the loss of effective heat transfer area.

It is worth noting that very high pressures (exceeding 100 MPa) corresponding to exceptionally high TCC values (surpassing 100 W/(mm^2·K)) may raise questions because such high pressures already greatly surpass the rupture stress (around 200 psi or 1.38 MPa) [40] or the ultimate shear strength (approximately 2.1 MPa) [41]. Consequently, the excessive pressure could lead to the formation of microvoids or cracks near the contact face, potentially reducing the TCC. For comparison, in the WT case, if we were to assign a TCC value of zero to all locations with pressures exceeding the rupture stress (1.38 MPa), the apparent TCC from crystal to copper would dramatically diminish to 0.0031 W/(mm^2·K). This value closely aligns with the regularly measured experimental value, typically around 0.002 W/(mm^2·K) in beamline exper-

25 August 2025 17:57:44

ACCEPTED MANUSCRIPT
Review of Scientific Instruments
AIP Publishing
This is the author's peer reviewed, accepted manuscript. However, the online version of record will be different from this version once it has been copyedited and typeset.
PLEASE CITE THIS ARTICLE AS DOI: 10.1063/5.0191095
25 August 2025 17:57:44

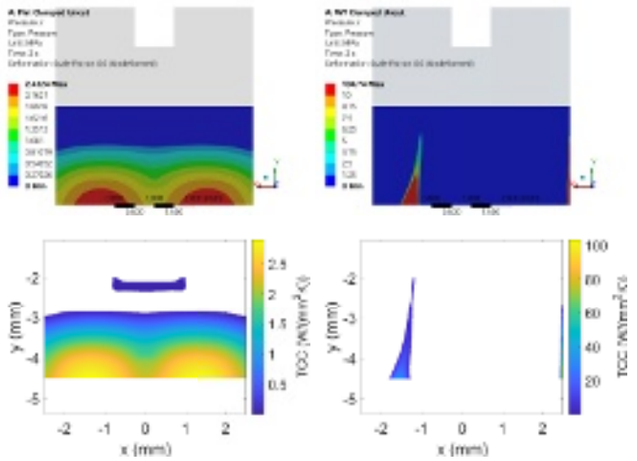

FIG. 6: Pressure (upper row) and TCC (lower row) distribution on C/In interface for flat case (left) and WT case (right) in clamped case.

imental stations. A more in-depth exploration of this intricate issue lies beyond the scope of this paper and will be considered in future studies.

TABLE I: Average TCC (W/(mm^2·K)) over apparent contact area for all cases

	Clamped		Hybrid	
	C/In	In/Cu	C/In	In/Cu
Flat uncut	1.03	0.93	1.41	1.13
WT uncut	0.55	0.50	1.10	0.96
WT cut	0.72	0.59	1.05	0.90

VI. COOLING PERFORMANCE

To gauge the cooling performance, we first calculate the effective TCC by averaging it over the effective contact area, thus yielding a single averaged value for subsequent steady-state thermal simulations. Importantly, we import the deformed geometry obtained from the static structural simulation to account for the corresponding contact conditions. Employing the thermal boundary conditions described in Section III, we can now simulate the temperature field. As an example, Fig. 7 illustrates the temperature field for the WT clamped case. The highest temperature is observed at the center of the XFEL spot, increases from the operational temperature 90 K to 186.74 K. The maximum temperatures for all other cases are summarized in Table II.

Table II reveals that the cooling performance remains similar across all three different thermal contact methods. However, the inclusion of surface profile imperfections into the simulation highlights a significant difference in XFEL spot temperature. In terms of temperature, the soldered case emerges as the most favorable, followed by the hybrid design.

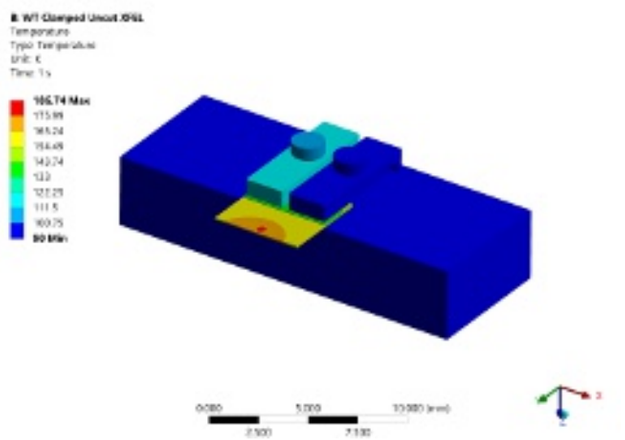

FIG. 7: Temperature field of WT clamped case. The temperature near XFEL footprint (maximal 186.74 K) is significantly higher than the cryocooled temperature of 90 K, as compared to 116.42 K in flat clamped case. The large difference is resulted from the loss of effective heat transfer area due to surface waviness and tilting.

TABLE II: Maximal temperature for all cases

	Clamped	Soldered	Hybrid
Flat uncut	116.42 K	114.73 K	117.16 K
WT uncut	186.74 K	112.71 K	117.23 K
WT cut	141.72 K	117.99 K	122.91 K

Nonetheless, it's crucial to emphasize that the mounting distortion is worst in the soldered case as described in Section IV.

We can extract the surface slope and total strain from the final static structural simulation, as demonstrated in Fig. 8. Here, we focus on the WT cases, as the flat cases significantly underestimate the distortion. After cooling to cryogenic temperatures, additional distortion is generated, especially at the soldered interface due to CTE mismatch. The solder shrinks much more than the diamond crystal or base, and since it is bonded to both the diamond crystal and the base, no sliding is allowed. Consequently, it effectively "grips" both parts, leading to crystal warpage. In contrast, the distortion for the clamped interface is not as pronounced because relative sliding is possible. Additionally, splitting the soldered area into two parts helps mitigate the "griping" effect of the solder over a long distance on the crystal, without losing much thermal contact area.

As illustrated in the left column of Fig. 8, the WT cases without strain-relief cuts under XFEL heating and cryogenic cooling exhibit significant surface slope variations. For the clamped case, the RMS surface slope is 156.02 μrad (varying from -312.09 μrad to 308.68 μrad). For the soldered case, the RMS surface slope is 5.15 μrad (varying from -13.20 μrad to 12.49 μrad). Meanwhile, for the hybrid case, the RMS surface slope is 6.46 μrad (varying from -9.07 μrad to 15.45 μrad). The clamping of the base to the holder in the

ACCEPTED MANUSCRIPT
Review of Scientific Instruments
AIP Publishing
This is the author's peer reviewed, accepted manuscript. However, the online version of record will be different from this version once it has been copyedited and typeset.
PLEASE CITE THIS ARTICLE AS DOI: 10.1063/5.0191095

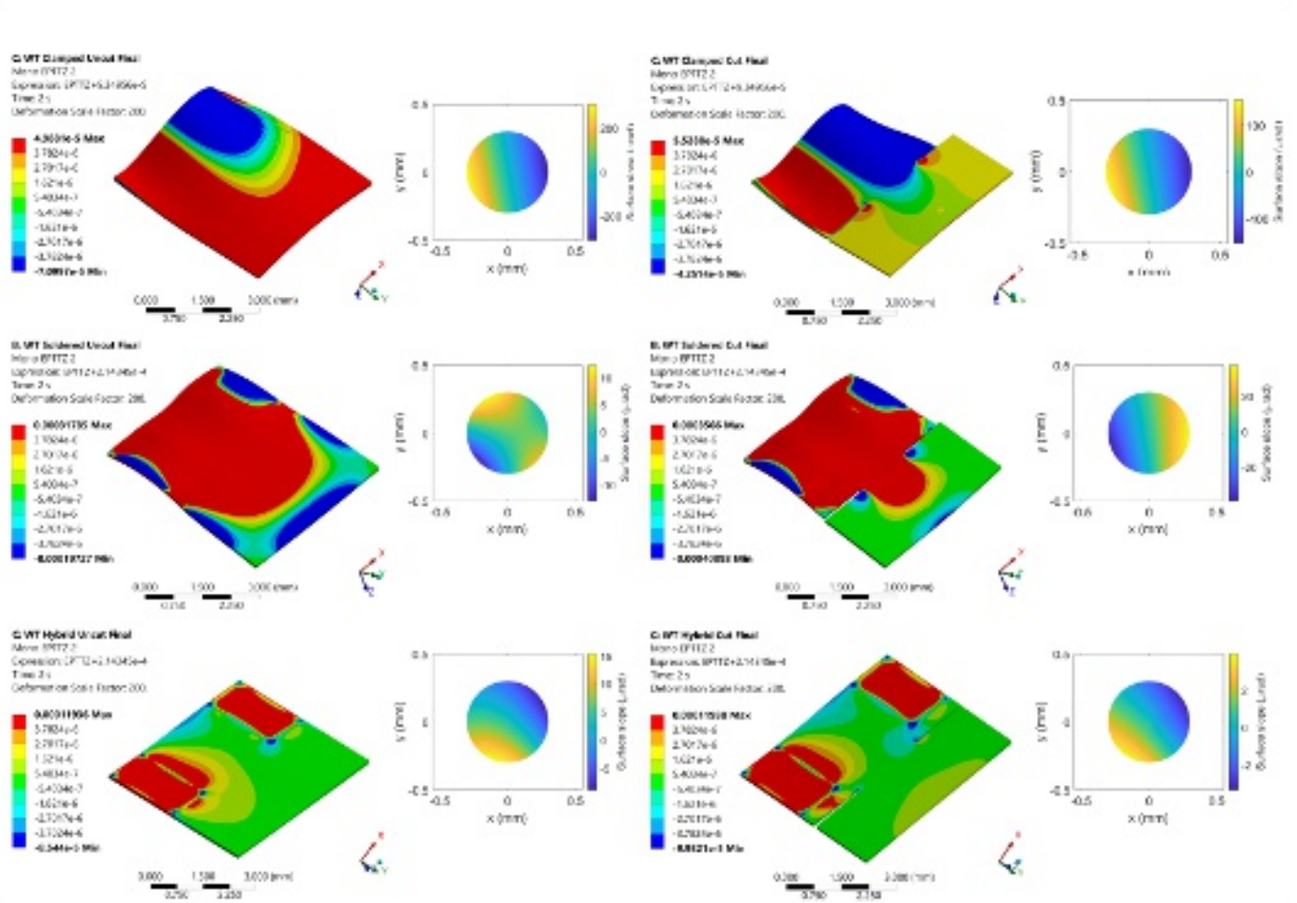

FIG. 8: Strain and surface slope of WT geometry for clamped (upper row), soldered (middle row) and hybrid (right row) cases. Without strain relief cut cases (left column) and with strian relief cut (right column). The colorbar for strain plot is modified to mostly show the strain within a Darwin width range of $\pm 3.78 \times 10^{-6}$. The circular region radius is 5 times of 3σ to show the surface slope near the beam center location. The strain field is offset by a reference strain (thermal strain of 9.34956×10^{-5} from 300 K to 90 K for clamped case, and 2.14345×10^{-4} from 391.15 K to 90 K for other cases) for better illustration.

hybrid case, as opposed to soldering the base in the soldered case, demonstrates superiority because it allows the base and holder to slide when cooled down and shrink, while still maintaining a reasonable TCC for efficient heat transfer.

The strain in ROI becomes elevated due to the large temperature decrease from 300 K. Its RMS in ROI is 2.69×10^{-6}, 3.20×10^{-6}, 3.66×10^{-7} for the clamped, soldered, and hybrid cases, respectively. The diamond base effectively shields the thin crystal from mounting distortion.

To further mitigate the distortion, strain relief cuts are introduced to the crystal near the two edges. These two cuts are 2.16 mm away from the front edge of the crystal. They are symmetric on each side of the crystal with a cut length of 1.5 mm and cut width of 0.08 mm. Unlike existing zigzag-shaped strain relief cuts, the proposed strain relief cuts maintain a short thermal path from the XFEL footprint to the thermal contact area while mitigating the warpage effect as much as possible. The results with strain relief cuts are presented in the right column of Fig. 8.

An intriguing finding is that the proposed strain relief cuts do offer an improvement in distortion for the clamped case but exacerbate the distortion for the soldered case. The proposed strain relief cuts undermine the strength of the thin crystal, which is the major resistance to the "griping" effect from the solder. Although some mitigation can be expected near the two corners on the free end, more bending could happen in the ROI, leading to more mounting distortion.

Overall, for the clamped case, the strain relief cuts mitigate the distortion by about 50%, but the distortion is still 10-100 times larger than the Darwin width at 9.83 keV. For the soldered case, the total strain in ROI is reduced to a RMS of 1.47×10^{-6}, but the surface slope varies much larger than the Darwin width at 9.83 keV. Moreover, compared to the uncut soldered case, the surface slope becomes even worse since the strain relief cuts reduce the thin crystal's strength. For the hybrid case, after the strain relief cuts, the surface slope and total strain are significantly reduced to a level that falls within the full width at half maximum (FWHM) of the rocking curve.

25 August 2025 17:57:44

ACCEPTED MANUSCRIPT
Review of Scientific Instruments
AIP Publishing
This is the author's peer reviewed, accepted manuscript. However, the online version of record will be different from this version once it has been copyedited and typeset.
PLEASE CITE THIS ARTICLE AS DOI: 10.1063/5.0191095

The strain is further reduced with a RMS of 4.11×10^{-8}. In sum, the hybrid case with strain relief cuts demonstrates sufficient distortion mitigation performance to reduce the distortion near the XFEL spot to an acceptable level. All results are also summarized in Table III.

It is worth noting that, compared to mounting distortion, non-uniform thermal distortion due to XFEL heating is secondary, as a very efficient thermal contact has been established. The thermal distortion can be observed in cases with strain relief cuts, for example, as a circular contour in the WT clamped cut case. This is expected to hold true for thermal load power lower than 15 W. However, it is important to acknowledge that accurately modeling the TCC is very complex, and XFEL thermal distortion could still dominate the overall system behavior, as observed in our previous works. Furthermore, the XFEL thermal distortion can also dominate if the thermal load power increases in certain applications.

VII. DISCUSSIONS

As demonstrated in this study, TCC is highly sensitive to the actual geometry profile of the contact faces. Measuring the precise profile of the contact faces within a certain level of precision is a challenging if not impossible task, which complicates the modeling of TCC for specific cases. Surface roughness can directly impact TCC through Eq. (1). However, the surface profile, including waviness and tilting, can have a more straightforward impact by limiting the effective heat transfer area. Even though local TCC can be very high according to Eq. (1), assuming rupture has no impact, the limited effective heat transfer area can restrict heat dissipation, potentially resulting in elevated temperatures at the XFEL footprint. This could be a contributing factor explaining why there are relatively few modeling studies addressing this issue.

For the further development of the system, several factors require additional optimization and investigation to enhance thermal performance. One critical factor is the non-diffusive thermal conductivity of the diamond thin plate. This characteristic has been explored in multiple works [42–45], and its impact can be significant due to the thinness of the diamond crystal and the low operating temperatures in cryogenic cooling. Further studies are needed to optimize the system's operating temperature while accounting for the non-diffusive thermal conductivity of the diamond.

Additionally, the dimension and location of the strain relief cuts require further optimization. It is important to note that as the size of the cuts increases and they approach the XFEL beam footprint, the thermal resistance of the crystal itself will also increase. Fig. 9 presents a comparison between an uncut crystal and a crystal with strain relief cuts. The crystal with strain relief cuts exhibits a slightly higher thermal resistance, approximately 30% higher than that of the uncut crystal. Experimental validation of the design should be carried out, evaluating distortion using techniques like rocking curve imaging [25, 26, 46–49]. These experimental validations will provide critical insights regarding the effectiveness of the strain relief cuts in reducing distortion. In addition, an alternative approach to achieve a potentially efficient cooling with drumhead structure crystal [23, 26, 50, 51] is also emerging as a very interesting option for high heat load scenario.

Moreover, there are additional concerns to address, including the vibration of the cryogenic cooler or the liquid nitrogen cooling system, the design compatibility of the motion system for the crystal, and the potential thermal fatigue of the mounting design. These factors are currently under investigation and will be reported in future articles, offering valuable insights into the overall performance of the thin-film X-ray optics.

VIII. CONCLUDING REMARKS

In summary, this study thoroughly investigated three mounting techniques—clamping, soldering, and a hybrid of clamping and soldering—specifically tailored for cryogenically cooled thin diamond crystals crucial in high-intensity XFEL applications. Clamping demonstrated resilience to temperature variations and allowed surface adjustments, yet demanded meticulous design to prevent stress concentration and loss of thermal contact. Conversely, soldering offered reliable mechanical and thermal bonding but encountered challenges related to temperature-induced expansion mismatches.

The hybrid approach, combining clamping and soldering with strategically placed strain relief cuts, effectively mitigated overall distortion caused by both the mounting process and XFEL-induced thermal loads. These findings provide indispensable insights into the intricate design requirements essential for mounting cryogenically cooled thin diamond crystals in high-intensity XFEL applications. They form a cornerstone guideline for the development of robust, high-performance mounting solutions, thereby propelling the advancement of cutting-edge X-ray optics and significantly contributing to the progress of XFEL research and its diverse applications.

IX. ACKNOWLEDGEMENTS

The work was supported by the Accelerator & Detector Research program of US Department of Energy (DOE) under contract DE-SC0023279.

[1] P. Emma, R. Akre, J. Arthur, R. Bionta, C. Bostedt, J. Bozek, A. Brachmann, P. Bucksbaum, R. Coffee, F.-J. Decker, *et al.*, nature photonics **4**, 641 (2010).

[2] T. Ishikawa, H. Aoyagi, T. Asaka, Y. Asano, N. Azumi, T. Bizen, H. Ego, K. Fukami, T. Fukui, Y. Furukawa, *et al.*, nature photonics **6**, 540 (2012).

25 August 2025 17:57:44

TABLE III: Summary of surface slope and strain for all cases

	Surface slope (μrad)			Strain		
	min	max	RMS	min	max	RMS
Flat clamped uncut 300 K	-3.62	3.58	1.78	-1.26×10^{-7}	1.58×10^{-8}	6.98×10^{-8}
Flat soldered uncut 300 K	-19.33	19.38	9.71	-7.19×10^{-7}	2.24×10^{-6}	9.71×10^{-7}
Flat hybrid uncut 300 K	-1.60	1.60	0.80	4.90×10^{-8}	3.23×10^{-7}	1.93×10^{-7}
WT clamped uncut 300 K	-3.62	3.58	1.78	-1.26×10^{-7}	1.58×10^{-8}	6.98×10^{-7}
WT soldered uncut 300 K	-2.34	4.29	1.39	-6.69×10^{-7}	2.13×10^{-6}	9.73×10^{-7}
WT hybrid uncut 300 K	-11.46	11.74	5.78	-9.69×10^{-8}	2.63×10^{-7}	1.30×10^{-7}
WT clamped uncut cooled	-312.09	308.68	156.02	-4.79×10^{-6}	4.66×10^{-6}	2.69×10^{-6}
WT soldered uncut cooled	-13.20	12.49	5.15	-2.32×10^{-6}	7.00×10^{-6}	3.20×10^{-6}
WT hybrid uncut cooled	-9.07	15.45	6.46	2.57×10^{-8}	6.55×10^{-7}	3.66×10^{-7}
WT clamped cut cooled	-153.67	154.04	77.80	-2.22×10^{-6}	2.23×10^{-6}	1.21×10^{-6}
WT soldered cut cooled	-39.33	37.73	19.13	-2.42×10^{-6}	3.63×10^{-6}	1.47×10^{-6}
WT hybrid cut cooled	-3.72	4.19	1.78	-9.09×10^{-8}	8.93×10^{-8}	4.11×10^{-8}

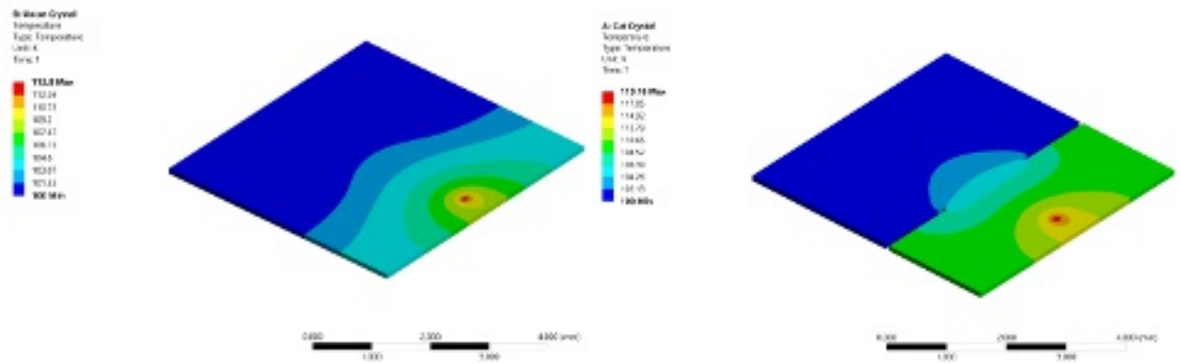

FIG. 9: Temperature field for crystals without (left) and with (right) strain relief cuts.

[3] H.-S. Kang, C.-K. Min, H. Heo, C. Kim, H. Yang, G. Kim, I. Nam, S. Y. Baek, H.-J. Choi, G. Mun, *et al.*, Nature Photonics **11**, 708 (2017).

[4] W. Decking, S. Abeghyan, P. Abramian, A. Abramsky, A. Aguirre, C. Albrecht, P. Alou, M. Altarelli, P. Altmann, K. Amyan, *et al.*, Nature Photonics **14**, 391 (2020).

[5] M. Smyth and J. Martin, Molecular Pathology **53**, 8 (2000).

[6] D. R. Powell, "Review of x-ray crystallography," (2016).

[7] L. X. Chen, X. Zhang, and M. Shelby, Chemical Science **5**, 4136 (2014).

[8] A. Plech, M. Wulff, S. Bratos, F. Mirloup, R. Vuilleumier, F. Schotte, and P. A. Anfinrud, Physical review letters **92**, 125505 (2004).

[9] I. A. Vartanyants, A. Singer, A. P. Mancuso, O. M. Yefanov, A. Sakdinawat, Y. Liu, E. Bang, G. J. Williams, G. Cadenazzi, B. Abbey, *et al.*, Physical review letters **107**, 144801 (2011).

[10] C. Gutt, P. Wochner, B. Fischer, H. Conrad, M. Castro-Colin, S. Lee, F. Lehmkühler, I. Steinke, M. Sprung, W. Roseker, *et al.*, Physical Review Letters **108**, 024801 (2012).

[11] G. Zhou, F.-J. Decker, Y. Ding, Y. Jiao, A. A. Lutman, T. J. Maxwell, T. O. Raubenheimer, J. Wang, A. J. Holman, C.-Y. Tsai, *et al.*, Scientific reports **10**, 1 (2020).

[12] Z. Qu, Y. Ma, G. Zhou, and J. Wu, Nuclear Instruments and Methods in Physics Research Section A: Accelerators, Spectrometers, Detectors and Associated Equipment **969**, 163936 (2020).

[13] Z. Qu, *Photo-thermo-mechanical analysis and control for high-brightness and high-repetition-rate x-ray optics*, Ph.D. thesis, UC Merced (2020).

[14] S. Liu, C. Grech, M. Guetg, S. Karabekyan, V. Kocharyan, N. Kujala, C. Lechner, T. Long, N. Mirian, W. Qin, S. Serkez, S. Tomin, J. Yan, S. Abeghyan, J. Anton, V. Blank, U. Boesenberg, F. Brinker, Y. Chen, W. Decking, X. Dong, S. Kearney, D. La Civita, A. Madsen, T. Maltezopoulos, A. Rodriguez-Fernandez, E. Saldin, L. Samoylova, M. Scholz, H. Sinn, V. Sleziona, D. Shu, T. Tanikawa, S. Terentiev, A. Trebushinin, T. Tschentscher, M. Vannoni, T. Wohlenberg, M. Yakopov, and G. Geloni, NATURE PHOTONICS (2023), 10.1038/s41566-023-01305.

[15] D. Zhu, Y. Feng, S. Stoupin, S. A. Terentyev, H. T. Lemke, D. M. Fritz, M. Chollet, J. Glownia, R. Alonso-Mori, M. Sikorski, *et al.*, Review of Scientific Instruments **85**, 063106 (2014).

[16] T. Osaka, M. Yabashi, Y. Sano, K. Tono, Y. Inubushi, T. Sato, S. Matsuyama, T. Ishikawa, and K. Yamauchi, Optics express **21**, 2823 (2013).

[17] D. Zhu, M. Cammarata, J. M. Feldkamp, D. M. Fritz, J. B. Hastings, S. Lee, H. T. Lemke, A. Robert, J. L. Turner, and Y. Feng, Applied Physics Letters **101** (2012).

[18] Y. Feng, D. Zhu, J. M. Feldkamp, H. T. Lemke, A. Robert, D. M. Fritz, M. Cammarata, S. Lee, J. B. Hastings, and J. L. Turner, in *X-Ray Free-Electron Lasers: Beam Diagnostics, Beamline Instrumentation, and Applications*, Vol. 8504 (SPIE,

ACCEPTED MANUSCRIPT

Review of Scientific Instruments

AIP Publishing

This is the author's peer reviewed, accepted manuscript. However, the online version of record will be different from this version once it has been copyedited and typeset.
PLEASE CITE THIS ARTICLE AS DOI: 10.1063/5.0191095

25 August 2025 17:57:44

ACCEPTED MANUSCRIPT
Review of Scientific Instruments
AIP Publishing
This is the author's peer reviewed, accepted manuscript. However, the online version of record will be different from this version once it has been copyedited and typeset.
PLEASE CITE THIS ARTICLE AS DOI: 10.1063/5.0191095

2012) pp. 131–139.
[19] J. Amann, W. Berg, V. Blank, F.-J. Decker, Y. Ding, P. Emma, Y. Feng, J. Frisch, D. Fritz, J. Hastings, *et al.*, Nature photonics **6**, 693 (2012).
[20] I. Nam, C.-K. Min, B. Oh, G. Kim, D. Na, Y. J. Suh, H. Yang, M. H. Cho, C. Kim, M.-J. Kim, *et al.*, Nature Photonics , 1 (2021).
[21] G. Geloni, X. Dong, S. Karabekyan, D. La Civita, L. Samoylova, S. Serkez, R. Shayduk, H. Sinn, V. Sleziona, M. Vannoni, *et al.*, in *Proceedings of the 39th International Free-Electron Laser Conference*, PROCEEDING-2020-005 (JACoW Publishing, 2019) pp. 242–245.
[22] S. Stoupin, Diamond and related materials **49**, 39 (2014).
[23] T. Kolodziej, P. Vodnala, S. Terentyev, V. Blank, and Y. Shvyd'ko, Journal of Applied Crystallography **49**, 1240 (2016).
[24] Y. Shvyd'ko, V. Blank, and S. Terentyev, MRS Bulletin **42**, 437 (2017).
[25] P. Pradhan, M. Wojcik, X. Huang, E. Kasman, L. Assoufid, J. Anton, D. Shu, S. Terentyev, V. Blank, K.-J. Kim, *et al.*, Journal of Synchrotron Radiation **27**, 1553 (2020).
[26] P. Liu, P. Pradhan, X. Shi, D. Shu, K. Kauchha, Z. Qiao, K. Tamasaku, T. Osaka, D. Zhu, T. Sato, *et al.*, in *Advances in Metrology for X-Ray and EUV Optics X*, Vol. 12695 (SPIE, 2023) pp. 115–124.
[27] Z. Qu, Y. Ma, G. Zhou, and J. Wu, Optics Express **28**, 30075 (2020).
[28] S. Stoupin, S. Terentyev, V. Blank, Y. V. Shvyd'ko, K. Goetze, L. Assoufid, S. Polyakov, M. Kuznetsov, N. Kornilov, J. Katsoudas, *et al.*, Journal of applied crystallography **47**, 1329 (2014).
[29] T. Takiya, H. Sugiyama, X. Zhang, S. Shimada, K. Yamazato, A. Komura, and M. Ando, Review of scientific instruments **70**, 3523 (1999).
[30] T. Takeuchi, M. Tanaka, H. Ohashi, and S. Goto, in *Advances in X-Ray/EUV Optics and Components VIII*, Vol. 8848 (SPIE, 2013) pp. 252–257.
[31] P. Marion, L. Zhang, L. Vallet, and M. Lesourd, MEDSI-proc-04 **53** (2004).
[32] R. Zhang, J. Cai, Q. Wang, J. Li, Y. Hu, H. Du, and L. Li, Journal of Electronic Packaging **136**, 011012 (2014).
[33] R. Stoner, H. Maris, T. Anthony, and W. Banholzer, Physical Review Letters **68**, 1563 (1992).
[34] Z. Qu, V. Borzenets, G. Zhou, Y. Ma, and J. Wu, Review of Scientific Instruments **92**, 083904 (2021).
[35] Z. Qu, Y. Ma, G. Zhou, and J. Wu, Journal of Synchrotron Radiation **27**, 1725 (2020).
[36] M. M. Yovanovich, IEEE transactions on components and packaging technologies **28**, 182 (2005).
[37] X. Cai, X. Yang, and P. Zhou, Journal of materials science letters **16**, 741 (1997).
[38] M. A. Lambert and L. S. Fletcher, Journal of Heat Transfer **119**, 684 (1997), https://asmedigitalcollection.asme.org/heattransfer/article-pdf/119/4/684/5910910/684_1.pdf.
[39] J. Zheng, Y. Li, L. Wang, and H. Tan, Cryogenics **61**, 133 (2014).
[40] L. J. Reitsma Jr, *A study of the recrystallization and the mechanical properties of indium*, Ph.D. thesis, Missouri University of Science and Technology (1959).
[41] M. Plötner, B. Donat, and A. Benke, Cryogenics **31**, 159 (1991).
[42] H.-B. Chae, Y.-J. Han, D.-J. Seong, J.-C. Kim, and Y.-J. Baik, Journal of applied physics **78**, 6849 (1995).
[43] J. Zemella, J. Rossbach, C. Maag, H. Sinn, and M. Tolkiehn, in *FEL 2012—34th International Free Electron Laser Conference*, Vol. 429 (2012).
[44] C. Maag, *Influence of pulsed heat load on the performance of diamond bragg mirrors for an xfel-oscillator*, Ph.D. thesis, Staats-und Universitätsbibliothek Hamburg Carl von Ossietzky (2018).
[45] Z. Qu, Y. Ma, G. Zhou, and J. Wu, Journal of Applied Physics **130**, 144503 (2021).
[46] A. Halavanau, J. MacArthur, R. Margraf, Z. Qu, G. Marcus, T. Sato, D. Zhu, C. Takacs, R. Arthur, B. Johnson, *et al.*, Proc. IPAC'21 , 357 (2021).
[47] A. Halavanau, R. Margraf, R. Robles, J. MacArthur, Z. Qu, G. Marcus, J. Wu, T. Sato, D. Zhu, C. J. Takacs, *et al.*, Journal of Applied Crystallography **56** (2023).
[48] D. Lübbert, T. Baumbach, J. Härtwig, E. Boller, and E. Pernot, Nuclear Instruments and Methods in Physics Research Section B: Beam Interactions with Materials and Atoms **160**, 521 (2000).
[49] S. Stoupin, Y. Shvyd'ko, E. Trakhtenberg, Z. Liu, K. Lang, X. Huang, M. Wieczorek, E. Kasman, J. Hammonds, A. Macrander, *et al.*, in *AIP Conference Proceedings*, Vol. 1741 (AIP Publishing, 2016).
[50] P. Pradhan, S. Antipov, Y. Shvyd, *et al.*, in *Advances in X-Ray/EUV Optics and Components XVII*, Vol. 12240 (SPIE, 2022) pp. 77–82.
[51] Y. Shvyd'ko, S. Terentyev, V. Blank, and T. Kolodziej, Journal of Synchrotron Radiation **28**, 1720 (2021).

25 August 2025 17:57:44